

A Spectral Method for Unbounded Domains

T. Matsushima and P. S. Marcus

*Department of Mechanical Engineering, University of California at Berkeley,
Berkeley, California 94720*

E-mail: phil@cfm.me.berkeley.edu

Received June 13, 1996; revised July 10, 1997

A spectral method for an unbounded domain is presented. Rational basis functions, which are algebraically mapped Legendre functions, are used for expansion in the radial direction of polar coordinates (r, ϕ) or (r, ϕ, z) . They satisfy the pole condition exactly at the coordinate singularity and their behavior as $r \rightarrow \infty$ is suitable for expanding smooth functions which decay algebraically or exponentially as $r \rightarrow \infty$. The method is not stiff when it is applied to initial value problems despite the presence of the coordinate singularity. Solenoidal vector fields are treated efficiently by the toroidal and poloidal decomposition which reduces the number of dependent variables from 3 to 2. Examples include the computation of vortex dynamics in two and three dimensions. © 1997 Academic Press

Key Words: spectral methods; unbounded domain.

1. INTRODUCTION

In our recent work [1] we developed a set of basis functions to expand analytic functions on the unit disk. For the radial part of the expansion we used the orthogonal polynomial eigenfunctions of a singular Sturm–Liouville equation. Here we consider a basis function set suitable for unbounded domains where the domain of r in polar coordinates (r, ϕ) or (r, ϕ, z) is $0 \leq r < \infty$. We require the basis functions to satisfy the pole condition [1] exactly at the coordinate singularity and to remain bounded as $r \rightarrow \infty$. To satisfy these requirements, rational functions are considered instead of polynomials.

To construct a basis function set for unbounded domains, it is necessary to assume the asymptotic behavior of the approximated functions for large r . The oscillatory behavior was treated, for example, by Rawitscher [2]. Here we assume that the

functions decay algebraically or exponentially for large r . One way to treat this class of functions is to map them to a bounded domain so that standard spectral basis functions such as the Chebyshev polynomials can be used. Grosch and Orszag [3] investigated the exponential and algebraic mapping methods and found by numerical experiments that the algebraic mapping gives a better result than the exponential mapping. Boyd [4] supported their result by examining the asymptotic behavior of the expansion coefficients of model functions by the method of steepest descent.

In spite of these investigations, however, the algebraic mapping has not excluded the use of exponential mapping. For example, an extra function can be included in the basis functions to represent the far field behavior of the expanded functions more efficiently [5, 6].

If the approximated functions decay exponentially as $r \rightarrow \infty$, there are many options for the basis functions. The sinc functions, Hermite functions, and Laguerre functions are the basis functions suitable for expanding functions which decay exponentially as $r \rightarrow \infty$ [7]. The domain truncation method, which imposes artificial boundary conditions at a sufficiently large radius, is also an efficient method [8–11]. The method can be made more efficient if additional mappings are used. For these cases the error can be made exponentially small even if the asymptotic behavior of the basis functions differs from that of approximated functions because the approximated functions are exponentially small for large r .

However, if approximated functions decay only algebraically, the exponentially decaying basis functions cannot be used efficiently [7]. The domain truncation method needs a very large truncation point to reduce the error which results from the artificial outer boundary conditions. To treat this class of functions Boyd [12] defined the rational Chebyshev functions $TL_n(r)$ on $0 \leq r < \infty$ by applying an algebraic mapping to the Chebyshev polynomials. The rational Chebyshev functions can expand functions which decay algebraically or exponentially for large r efficiently. However, the $TL_n(r)$ are not designed to satisfy the pole condition and will cause stiffness in time-dependent problems if they are used for expansions in the radial direction in polar coordinates.

Basis functions presented here are algebraically mapped Legendre functions. They satisfy the pole condition exactly at the origin, behave algebraically as $r \rightarrow \infty$, and are suitable for expanding functions which decay algebraically or exponentially as $r \rightarrow \infty$. They can be used to expand vector functions efficiently by using the toroidal and poloidal decomposition [13–15].

One important application of our method is the computation of vortex dynamics in an unbounded domain. For this problem, the Lagrangian vortex method [16–18] is very popular because it naturally treats the boundary condition at infinity correctly. Our method also treats the condition correctly and is efficient because the fast Fourier transform can be used naturally in mapping the azimuthal direction. Thus it offers an alternative method to the vortex methods.

We develop the basis functions in Section 2. Vector fields are treated in Section 3. The application of the basis functions will be illustrated through some examples in Section 4.

2. RATIONAL LEGENDRE FUNCTIONS

Consider the basis functions to expand $f_m(r)$ when a C^∞ scalar function $f(r, \phi)$ is represented as a Fourier series in ϕ

$$f(r, \phi) = \sum_{m=-\infty}^{\infty} f_m(r)e^{im\phi}, \tag{1}$$

where $0 \leq r < \infty$ and $0 \leq \phi < 2\pi$. The pole condition is that $f_m(r) \rightarrow O(r^{|m|+2p})$ as $r \rightarrow 0$ for a nonnegative integer p . We shall assume that $f_m(r)$ decays as $O(r^{-|m|-2p})$ or faster (e.g., exponentially) as $r \rightarrow \infty$. As we show in Section 4, this behavior is appropriate for the computation of vortex dynamics in an unbounded domain.

To expand this class of functions, we consider the mapping of the associated Legendre functions $P_n^m(\mu)$ [19] by

$$r = L \sqrt{\frac{1 + \mu}{1 - \mu}} \tag{2}$$

or

$$\mu = \frac{r^2 - L^2}{r^2 + L^2}, \tag{3}$$

where $L > 0$ is the map parameter which can be adjusted to optimize the convergence of the expansion. The interval $-1 \leq \mu < 1$ on which the Legendre functions are orthogonal is mapped to $0 \leq r < \infty$. We define the mapped function as

$$P_{L_n}^m(r) \equiv P_n^m(\mu(r)). \tag{4}$$

The behavior of $P_{L_n}^m(r)$ can be examined by applying (2) to the relation between $P_n^m(\mu)$ and $P_n^0(r)$ [19] as

$$P_{L_n}^m(r) = \frac{r^{|m|}L^{|m|}}{(L^2 + r^2)^{|m|}} G_n^m(r), \tag{5}$$

where

$$G_n^m(r) \equiv (-1)^m \left(\frac{(L^2 + r^2)^2}{2L^2r} \frac{d}{dr} \right)^{|m|} P_{L_n}^0(r). \tag{6}$$

The $G_n^m(r)$ is an even function and behaves as $O(1)$ for $r \rightarrow 0$ and $r \rightarrow \infty$. Thus a $P_{L_n}^m(r)$ is an even (odd) function of r if m is even (odd). Equation (5) shows that $P_{L_n}^m(r)$ behaves as

$$P_{L_n}^m(r) = O(r^{|m|}), \quad r \rightarrow 0 \tag{7}$$

$$P_{L_n}^m(r) = O(r^{-|m|}), \quad r \rightarrow \infty. \tag{8}$$

Using $P_{L_n}^m(r)$, we expand $f_m(r)$ in (1) as

$$f_m(r) = \sum_{n=|m|}^{\infty} f_n^m P_{L_n}^m(r). \tag{9}$$

By (7) and (8) each basis function $P_{L_n}^m(r)e^{im\phi}$ in the double sum in (1) and (9) behaves as C^∞ at $r = 0$ and $O(r^{-|m|}e^{im\phi})$ or *harmonically* as $r \rightarrow \infty$.

The differential equation which the $P_{L_n}^m(r)$ satisfies can be obtained by writing the Legendre equation in terms of r as

$$\frac{1}{r} \frac{d}{dr} r \frac{d}{dr} P_{L_n}^m(r) - \frac{m^2}{r^2} P_{L_n}^m(r) + \frac{4n(n+1)L^2}{(L^2 + r^2)^2} P_{L_n}^m(r) = 0. \tag{10}$$

Equation (10) has regular singularities at $r = 0, \pm iL$, and ∞ . Because (10) is a Sturm–Liouville equation, the set of $P_{L_n}^m(r)$ for fixed integer m and $n = |m|, |m| + 1, \dots, \infty$ is complete and orthogonal with respect to the weight function

$$w(r) \equiv \frac{4L^2 r}{(L^2 + r^2)^2}. \tag{11}$$

Therefore

$$\int_0^\infty P_{L_n}^m(r) P_{L_{n'}}^m(r) w(r) dr = \int_{-1}^1 P_n^m(\mu) P_{n'}^m(\mu) d\mu = (N_n^m)^2 \delta_{nn'}, \tag{12}$$

where

$$N_n^m = \left(\frac{2(n + |m|)!}{(2n + 1)(n - |m|)!} \right)^{1/2}. \tag{13}$$

Note the appearance of the two-dimensional Laplacian for the m th azimuthal Fourier component in (10)

$$\nabla_{\perp}^2(m) \equiv \frac{1}{r} \frac{d}{dr} r \frac{d}{dr} - \frac{m^2}{r^2}. \tag{14}$$

(We denote the two-dimensional Laplacian by $\nabla_{\perp}^2(m)$ to distinguish it from the three-dimensional Laplacian $\nabla^2(m, k)$. See Section 3.)

The expansion coefficients in (9) can be obtained by using the orthogonality (12) as

$$f_n^m = \frac{1}{(N_n^m)^2} \int_0^\infty f_m(r) P_{L_n}^m(r) w(r) dr. \tag{15}$$

For vector functions, the procedure to obtain the expansion coefficients is slightly more complicated and for later use we derive a formula using (10), (12), and (14) as

TABLE I
The Rational Legendre Functions
($L = 1$)

$P_{L_0}^0(r) = 1$
$P_{L_1}^0(r) = (r^2 - 1)/(r^2 + 1)$
$P_{L_2}^0(r) = (r^4 - 4r^2 + 1)/(r^2 + 1)^2$
$P_{L_3}^0(r) = (r^6 - 9r^4 + 9r^2 - 1)/(r^2 + 1)^3$
$P_{L_1}^1(r) = -2r/(r^2 + 1)$
$P_{L_2}^1(r) = -6r(r^2 - 1)/(r^2 + 1)^2$
$P_{L_3}^1(r) = -12r(r^4 - 3r^2 + 1)/(r^2 + 1)^3$
$P_{L_2}^2(r) = 12r^2/(r^2 + 1)^2$
$P_{L_3}^2(r) = 60r^2(r^2 - 1)/(r^2 + 1)^3$
$P_{L_3}^3(r) = -120r^3/(r^2 + 1)^3$

$$\int_0^\infty P_{L_n}^m(r)(\nabla_\perp^2(m)P_{L_n}^m(r))r dr = -n(n + 1)(N_n^m)^2 \delta_{mm'}. \tag{16}$$

In particular

$$\int_0^\infty (\nabla_\perp^2(0)P_{L_n}^0(r))r dr = 0 \tag{17}$$

because $P_{L_0}^0(r) = 1$. Note that (16) does not imply that $P_{L_n}^m(r)$ is an eigenfunction of $\nabla_\perp^2(m)$ because the weight function $w(r)$ which appears in (12) is missing in (16).

The spectral convergence of the expansion coefficients in (15) for C^∞ functions $f_m(r)$ with the property that as $r \rightarrow \infty$, $(d/dr)f_m(r) = O(r^{-p})$, where p is integer and $p \geq 2$, can be proved by the standard method [20] by using the fact that as $r \rightarrow \infty$, $(d/dr)P_{L_n}^m(r) = O(r^{-p})$. The convergence is also spectral for C^∞ functions $f_m(r)$ if $f_m(r)$ decays exponentially as $r \rightarrow \infty$.

The $P_{L_n}^m(r)$ can be evaluated by the standard recurrence relations to evaluate the associated Legendre functions [21]. Some $P_{L_n}^m(r)$ are shown in Table I. We call these functions the ‘‘rational Legendre functions.’’

At this point a few comments are worth noting. Consider the truncated series of (1) and (9)

$$f_M(r, \phi) \equiv \sum_{m=-M}^M \tilde{f}_m(r)e^{im\phi} \equiv \sum_{m=-M}^M \sum_{n=|m|}^M f_n^m P_{L_n}^m(r)e^{im\phi}. \tag{18}$$

It is easy to prove the following: If $f_M(r, \phi)$ is integrable (over the entire physical domain), then $\tilde{f}_0(r)$ must decay as fast or faster than $O(r^{-4})$ as $r \rightarrow \infty$, or equivalently, the polynomial $\tilde{f}_0(r(\mu))$ must be divisible by $(1 - \mu)^2$. *Proof:* The integral of $f_M(r, \phi)$ is

$$\int_0^{2\pi} \int_0^\infty f_M(r, \phi) r dr d\phi = 2\pi \int_0^\infty \tilde{f}_0 r dr = 2\pi L^2 \int_{-1}^1 \frac{\tilde{f}_0(r(\mu))}{(1 - \mu)^2} d\mu. \tag{19}$$

Note that $\tilde{f}_0(r(\mu))$ is a polynomial in μ due to the second equality in (18), the definition (4), and the properties of the $m = 0$ associated Legendre polynomials.

In order to evaluate integrals with $\tilde{f}_m(r)$ in their integrands, we use Gaussian quadrature where the radial collocation points $\{r_i\}$, $1 \leq i \leq M$, are related to the standard [21] Gauss–Legendre abscissas μ_i on the interval $-1 \leq \mu \leq 1$ by Eq. (2). However, we can reduce the work in evaluating $\tilde{f}_m(r_i)$ by half by exploiting the even and odd parity of the associated Legendre functions about $\mu = 0$. We define

$$\tilde{f}_m^+(r_i) \equiv \sum_{\substack{n=|m| \\ n+m \text{ even}}}^M f_n^m P_n^m(r_i), \quad 1 \leq i \leq \frac{M}{2} \tag{20}$$

$$\tilde{f}_m^-(r_i) \equiv \sum_{\substack{n=|m|+1 \\ n+m \text{ odd}}}^M f_n^m P_n^m(r_i), \quad 1 \leq i \leq \frac{M}{2}. \tag{21}$$

Then, for even M (there are similar expressions for odd M),

$$\tilde{f}_m(r_i) = \tilde{f}_m^+(r_i) + \tilde{f}_m^-(r_i), \quad 1 \leq i \leq \frac{M}{2} \tag{22}$$

$$\tilde{f}_m(r_i) = \tilde{f}_m^+(r_{M-i+1}) - \tilde{f}_m^-(r_{M-i+1}), \quad \frac{M}{2} + 1 \leq i \leq M. \tag{23}$$

A similar procedure can be used to find f_n^m from $\tilde{f}_m(r_i)$.

To better understand the resolution properties of the $P_n^m(r)$ and to see how they relate to expansion functions used by other authors, we consider their relation to spherical harmonics. Equation (18) is directly related to the spherical harmonic expansion [21] in spherical coordinates (θ, ϕ) by (2), (4), and

$$\mu \equiv \cos \theta \tag{24}$$

as

$$f_M(\theta, \phi) = \sum_{m=-M}^M \sum_{n=|m|}^M \sqrt{2\pi} N_n^m f_n^m Y_n^m(\theta, \phi), \tag{25}$$

where

$$Y_n^m(\theta, \phi) = \frac{P_n^m(\cos \theta)}{\sqrt{2\pi} N_n^m} e^{im\phi}. \tag{26}$$

The mapping from the surface of the sphere to the (r, ϕ) plane defined by (2) and (24) is the *stereographic projection* [22]. Although the domain of expansion (18) is unbounded, the region where we can attain a reasonable resolution by the truncated rational Legendre–Fourier series is confined near the origin. To see this, we note that with the triangular truncation in (18), the resolution of the series (25) is uniform over the entire spherical surface [7, 23]. Thus the resolution of the expansion (18)

as a function of r can be estimated by the ratio of an infinitesimal area on the sphere $\sin \theta \, d\theta \, d\phi$ to the corresponding area $r \, dr \, d\phi$, that is

$$X_L \equiv \left| \frac{\sin \theta \, d\theta}{r \, dr} \right| = \frac{4L^2}{(r^2 + L^2)^2}. \tag{27}$$

Thus the resolution decreases as $O(r^{-4})$ as $r \rightarrow \infty$. The ratio of X_L to its value at the origin is $1/4$ at $r = L$ and $1/25$ at $r = 2L$. The resolution decreases rapidly for $r > L$. Because the interval $0 \leq r \leq L$ corresponds to the interval $-1 \leq \mu \leq 0$, half of the collocation points (with $\mu(r_i) < 0$ and $r_i < L$) are distributed in the high-resolution region and the other half are located in the low-resolution region ($r_i > L$).

If truncation other than triangular is used, the resolution property will be differently from (27). Another choice of truncation is to increase the number of radial modes for large $|m|$ in order to obtain better resolution for $r \sim L$ (i.e., instead of triangular truncation, we can replace the sums in (25), $\sum_{m=-M}^M \sum_{n=|m|}^M$ with $\sum_{m=-M}^M \sum_{n=|m|}^{M+|m|}$). However, in all of the examples in this paper only triangular truncation is used. We note that mapping functions similar to the stereographic projection have been applied to the Fourier series

$$g(\theta) = \sum_{n=0}^{\infty} a_n \cos(n\theta) + \sum_{n=1}^{\infty} b_n \sin(n\theta). \tag{28}$$

Cain *et al.* [24] considered the mapping

$$y = L \frac{\sin \theta}{1 - \cos \theta} = L \cot \frac{\theta}{2}, \tag{29}$$

where the interval $-\infty < y < \infty$ is mapped to $0 < \theta < 2\pi$. Note that with $\mu = \cos \theta$ and $r = y$, (29) is equivalent to (2). They considered another mapping

$$y = L \cot \theta \tag{30}$$

for which the interval $-\infty < y < \infty$ is mapped to $0 < \theta < \pi$. Boyd used (30) to define the rational Chebyshev functions $TB_n(y)$ [25]. One constraint of mapping (29) is that $g(\theta(y))$ needs to go to the same values as $y \rightarrow \infty$ and $y \rightarrow -\infty$ because it uses the full interval of the Fourier series. Otherwise, the series (28) has a Gibbs' phenomenon at $\theta = 0$ and 2π , and the exponential convergence of the series will be lost. On the other hand, (30) does not cause this problem. For Legendre functions, the stereographic projection does not lead to a Gibbs' problem because of the condition (8).

The resolution property of the rational Legendre–Fourier series presented in this paper is similar to that of Fourier series mapped by (29) or (30). For example, the resolution factor for mapping (29) can be defined similarly to (27) as $X_F \equiv |d\theta/dy| = 2L/(L^2 + y^2)$ because the resolution of the Fourier series (28) is uniform in θ . The resolution decreases as $O(y^{-2})$ as $y \rightarrow \pm\infty$ compared to $O(r^{-4})$ for the

expansion (18). The difference is due to the two-dimensional nature in the calculation of (27).

The mapping defined by (28) and (29) could be extended to two dimensions by applying it to each direction of Cartesian coordinates. However, evaluating the Laplace and Helmholtz operators and their inverses in this expansion is inefficient because the operators couple the two directions together; i.e., the operators written as matrices are not block diagonal. This cancels the advantage of the ability to use fast Fourier transform in both directions. On the other hand, even though our method using (18) needs a slow transform in one direction, the Laplace and Helmholtz operators are decoupled for each azimuthal Fourier component (i.e., block diagonal) and the inversion of each block is fast (order $M/2$). Moreover, Eq. (18) has the advantage that it is Galerkin, capturing the correct behavior at $r = 0$ and at $r \rightarrow \infty$, so no boundary conditions need to be imposed. It also has the advantage that it does not break rotational symmetry; thus the $P_{L_n}^m(r)$ are superior to the expansions of (28) and (29) in studying transitions where symmetry is important. Moreover our method is useful for computing the linearized perturbations of flows where the eigenmodes are proportional to $e^{im\phi}$ which is not easy with a Cartesian code.

3. VECTOR FIELDS

3.1. Components in Cartesian and Polar Coordinates

Because the three components of a vector field behave differently from a scalar field, it is generally not convenient to expand the components with a rational Legendre–Fourier series. The difficulties of treating the components in Cartesian and polar coordinates are discussed in this section, and a general method for treating vectors is presented. However, in axially periodic geometries, we believe the best method is vector decomposition into toroidal and poloidal components. This will be discussed in Section 3.2.

Consider the expansion of the components of a vector field \mathbf{u} in Cartesian and polar coordinates by the rational Legendre–Fourier series. We denote the Cartesian components by $u_x(r, \phi, z)$, $u_y(r, \phi, z)$, and $u_z(r, \phi, z)$ and the polar components by $u_r(r, \phi, z)$, $u_\phi(r, \phi, z)$, and $u_z(r, \phi, z)$. The x and y are related to r and ϕ by $x = r \cos \phi$ and $y = r \sin \phi$. The axial component $u_z(r, \phi, z)$ is identical in Cartesian and polar coordinates and no distinction is made. Expansion in the axial direction is not important here. Throughout this section we use the notation that $q_{,m} \equiv (1/2\pi) \int_0^{2\pi} q(\phi) e^{-im\phi} d\phi$ for any quantity $q(\phi)$.

To be C^∞ at the origin, it can be shown [1, 26] that $u_{\xi,m}$ behaves as $r^{|m|+2p}$ as $r \rightarrow 0$ for nonnegative integer p for $\xi = x, y$, and z . It can also be shown that as $r \rightarrow 0$

$$r(u_r - iu_\phi)_{,m} \rightarrow O(r^{m+2p}) \quad \text{for } m \geq 1 \tag{31}$$

$$r(u_r - iu_\phi)_{,m} \rightarrow O(r^{|m|+2p+2}) \quad \text{for } m \leq 0 \tag{32}$$

$$r(u_r + iu_\phi)_{,m} \rightarrow O(r^{m+2p+2}) \quad \text{for } m \geq 0 \tag{33}$$

$$r(u_r + iu_\phi)_{,m} \rightarrow O(r^{|m|+2p}) \quad \text{for } m \leq -1. \quad (34)$$

Equations (31)–(34) imply that as $r \rightarrow 0$

$$ru_{r,m} \rightarrow O(r^{|m|+2p}) \quad \text{for } |m| > 0 \quad (35)$$

$$ru_{\phi,m} \rightarrow O(r^{|m|+2p}) \quad \text{for } |m| > 0 \quad (36)$$

$$ru_{r,0} \rightarrow O(r^{2+2p}) \quad (37)$$

$$ru_{\phi,0} \rightarrow O(r^{2+2p}). \quad (38)$$

Note that Eqs. (35)–(38) do not imply (31)–(34) because they are less restrictive.

For the remainder of this paper we shall assume that the vector field decays and is harmonic at $r \rightarrow \infty$. Then as $r \rightarrow \infty$, it can be shown that the Cartesian components $u_{x,m}$, $u_{y,m}$, and $u_{z,m}$ behave as $O(r^{-|m|})$ and that

$$\lim_{r \rightarrow \infty} |m|r^{|m|}u_{x,m}(r, z) = \lim_{r \rightarrow \infty} im r^{|m|}u_{y,m}(r, z). \quad (39)$$

With polar components, the harmonic condition at $r \rightarrow \infty$ requires that $ru_{r,m}$ and $ru_{\phi,m}$ behave as $O(r^{-|m|})$ as $r \rightarrow \infty$ and that

$$\lim_{r \rightarrow \infty} |m|r^{|m|+1}u_{\phi,m}(r, z) = \lim_{r \rightarrow \infty} im r^{|m|+1}u_{r,m}(r, z). \quad (40)$$

Thus, a complete expansion for $u_{\xi,m}$ is

$$u_{\xi,m}(r, z) = \sum_{n=|m|}^{\infty} a_{mn}^{\xi}(z)P_{L_n}^m(r) \quad (41)$$

for $\xi = x, y$, and z subject to the constraint (39) and

$$ru_{\xi,m}(r, z) = \sum_{n=|m|}^{\infty} a_{mn}^{\xi}(z)P_{L_n}^m(r) \quad (42)$$

for $\xi = r$ and ϕ subject to the constraints (31)–(34) and (40).

The difficulty of using either polar or Cartesian vector components as computational variables in a truncated form of (41) or (42) is that the constraints (31)–(34), (39), and (40) involve all of the coefficients a_{mn}^{ξ} . For example, in a pseudo-spectral calculation the nonlinear advection term (e.g., $\boldsymbol{\omega} \times \mathbf{u}$) is usually computed in physical space at the collocation points, and the three components of the vector are then transformed into rational Legendre–Fourier space so that they are represented as in (41) or (42). If there is any aliasing error or if the series in (41) or (42) is truncated at a degree lower than that of the vector in physical space, then the transformed vector will not obey the pole constraints (31)–(34) nor the constraints at infinity (39) and (40) even if the nonlinear term in physical space does.

One way to avoid these difficulties is to define new variables

$$U = u_r + iu_\phi \quad (43)$$

$$V = u_r - iu_\phi. \tag{44}$$

Then one can show that there is no constraint coupling U and V . The variables are also known to simplify the vector Laplacian operator [27]. However, the toroidal and poloidal decomposition is an even better way to handle solenoidal vector fields because it reduces the number of variables from 3 to 2. It is described in the next section.

3.2. Toroidal and Poloidal Components

The toroidal and poloidal decomposition of solenoidal three-dimensional vector fields is discussed in Chandrasekhar [13] and has been applied to numerical simulations in spherical geometry by Marcus [14] and Glatzmaier [15]. We apply the decomposition in polar coordinates. For simplicity we assume that the vector fields are periodic in the axial direction with wavelength Z and their behavior as $r \rightarrow \infty$ is suited to the rational Legendre–Fourier expansion. The decomposition requires a reference vector and the unit vector in the axial direction \mathbf{z} is chosen. A vector field $\mathbf{u}(r, \phi, z) = (u_r, u_\phi, u_z)$ is written as

$$\mathbf{u} = \nabla \times (\psi \mathbf{z}) + \nabla \times \nabla \times (\chi \mathbf{z}), \tag{45}$$

where $\psi(r, \phi, z)$ is the toroidal component and $\chi(r, \phi, z)$ is the poloidal component. The \mathbf{u} is clearly solenoidal and it is represented by two scalars. If desired, we may add another vector field $\nabla \vartheta(r, \phi, z)$ to make the expression complete. In fact even if a solenoidal field is of interest, one usually has to include $\nabla \vartheta$, where $\vartheta(r, \phi, z)$ satisfies $\nabla^2 \vartheta = 0$ for completeness and to satisfy the boundary conditions. However, our domain has no boundary and with the assumption about the behavior of the vector fields as $r \rightarrow \infty$, no such additional behavior harmonic component is necessary.

Now note that the toroidal part $\nabla \times (\psi \mathbf{z})$ contains no axial component. Thus

$$\mathbf{u} \cdot \mathbf{z} = -\nabla_\perp^2 \chi. \tag{46}$$

Further, the curl of the poloidal part of \mathbf{u} contains no axial component. Thus

$$\boldsymbol{\omega} \cdot \mathbf{z} = -\nabla_\perp^2 \psi, \tag{47}$$

where $\boldsymbol{\omega} \equiv \nabla \times \mathbf{u}$.

The $\psi(r, \phi, z)$ and $\chi(r, \phi, z)$ in (45) can be expanded by the rational Legendre–Fourier series as

$$\psi(r, \phi, z) = \psi_0(r, \phi, z) + \psi_l P_l(r) \tag{48}$$

$$\chi(r, \phi, z) = \chi_0(r, \phi, z) + \chi_l P_l(r), \tag{49}$$

where

$$\psi_0(r, \phi, z) = \sum_{k=-\infty}^{\infty} \sum_{m=-\infty}^{\infty} \psi_{mk}(r) e^{im\phi + 2\pi ikz/Z} \quad (50)$$

$$\psi_{mk}(r) = \sum_{n=|m|}^{\infty} \psi_{mnk} P_{L_n}^m(r) \quad (51)$$

$$\chi_0(r, \phi, z) = \sum_{k=-\infty}^{\infty} \sum_{m=-\infty}^{\infty} \chi_{mk}(r) e^{im\phi + 2\pi ikz/Z} \quad (52)$$

$$\chi_{mk}(r) = \sum_{n=|m|}^{\infty} \chi_{mnk} P_{L_n}^m(r) \quad (53)$$

and

$$P_l(r) \equiv \ln \left(\frac{L^2 + r^2}{2L^2} \right). \quad (54)$$

The logarithmic terms ψ_l and χ_l are necessary for completeness; e.g., they account for the behavior $u_\phi \sim O(1/r)$ as $r \rightarrow \infty$ and for the mean axial components of $\boldsymbol{\omega}$ and \mathbf{u} (see below). The velocity vector defined by (45) automatically satisfies the constraints (31)–(34) at the origin and (40) at infinity.

The form of $P_l(r)$ is particularly convenient because its derivative has a simple relation with the rational Legendre functions, i.e.,

$$r \frac{dP_l(r)}{dr} = P_{L_1}^0(r) + P_{L_0}^0(r). \quad (55)$$

Important relations about ψ_l and χ_l can be derived by using (46), (47), and (17) as

$$\psi_l = -\frac{1}{4\pi Z} \int_0^Z dz \int_0^{2\pi} d\phi \int_0^\infty r dr \boldsymbol{\omega} \cdot \mathbf{z} \quad (56)$$

$$\chi_l = -\frac{1}{4\pi Z} \int_0^Z dz \int_0^{2\pi} d\phi \int_0^\infty r dr \mathbf{u} \cdot \mathbf{z} \quad (57)$$

Thus only ψ_l and χ_l are related to the integration of the z -components of $\boldsymbol{\omega}$ and \mathbf{u} . On the other hand, coefficients ψ_{00k} and χ_{00k} do not affect \mathbf{u} . We use this gauge freedom to satisfy

$$\lim_{r \rightarrow \infty} \psi_0(r, \phi, z) = 0 \quad (58)$$

$$\lim_{r \rightarrow \infty} \chi_0(r, \phi, z) = 0. \quad (59)$$

The components of \mathbf{u} can be computed straightforwardly at each collocation point if the expansion coefficients ψ_{mnk} , χ_{mnk} , ψ_l , and χ_l are given. To find the expansion coefficients from the vector components, first we find ψ_l by the relation

$$\psi_l = -\frac{1}{2} \lim_{r \rightarrow \infty} r u_{\phi,00}(r) \quad (60)$$

(we use the notation $q_{,mk} \equiv (1/2\pi Z) \int_0^Z \int_0^{2\pi} q(\phi, z) e^{-im\phi - 2\pi ikz/Z} d\phi dz$ for any $q(\phi, z)$). (Note that in many cases ψ_l is zero, e.g., if the vector field is the nonlinear advection term $\boldsymbol{\omega} \times \mathbf{u}$.) Subtracting the contribution from \mathbf{u} due to ψ_l , we define

$$\tilde{\mathbf{u}} \equiv \nabla \times (\psi_0 \mathbf{z}) + \nabla \times \nabla \times (\chi \mathbf{z}). \quad (61)$$

Then (46), (47), and (16) show that

$$\psi_{mnk} = \frac{1}{c_n} \int_0^Z dz \int_0^{2\pi} d\phi \int_0^\infty r dr \mathbf{f}_n^m \cdot (\nabla \times \tilde{\mathbf{u}}) \quad (62)$$

$$\chi'_{mnk} = -\frac{1}{c_n} \int_0^Z dz \int_0^{2\pi} d\phi \int_0^\infty r dr \mathbf{f}_n^m \cdot (\nabla \times \nabla \times \tilde{\mathbf{u}}) \quad (63)$$

or equivalently,

$$\psi_{mnk} = \frac{1}{c_n} \int_0^Z dz \int_0^{2\pi} d\phi \int_0^\infty r dr (\nabla \times \mathbf{f}_n^m) \cdot \tilde{\mathbf{u}} \quad (64)$$

$$\chi'_{mnk} = -\frac{1}{c_n} \int_0^Z dz \int_0^{2\pi} d\phi \int_0^\infty r dr (\nabla \times \nabla \times \mathbf{f}_n^m) \cdot \tilde{\mathbf{u}}, \quad (65)$$

where

$$c_n \equiv 2\pi Zn(n+1)(N_n^m)^2 \quad (66)$$

$$\mathbf{f}_n^m \equiv (P_{L_n}^m(r) e^{-im\phi - 2\pi ikz/Z}) \mathbf{z}. \quad (67)$$

The χ'_{mnk} are the rational Legendre–Fourier expansion coefficients of $\nabla^2 \chi$. Equations (64) and (65) follow from integration by parts and observation that the surface term $r(\mathbf{f}_n^m \times \tilde{\mathbf{u}})_r$ vanishes at infinity. In actual computation, we use (64) and (65) rather than (62) and (63) in order to avoid any inefficiency associated with the operations on the components of $\tilde{\mathbf{u}}$ (it is efficient to compute the curls of \mathbf{f}_n^m). We note that a similar method of using vector inner products was defined by Leonard and Wray [28].

The procedure of inverting the Laplacian to find χ_{mnk} and χ_l from χ'_{mnk} can be constructed easily by using the operators defined in the Appendix. The Laplacian has a banded structure and can be inverted inexpensively. Boundary conditions are not necessary because the basis functions are of Galerkin type. However, depending on the physical situations, a boundary condition can be imposed by the tau method (e.g., $\chi_l = 0$ for nonlinear term $\boldsymbol{\omega} \times \mathbf{u}$).

The computation of toroidal and poloidal components can be regarded as a projection into the solenoidal component of a given vector field. It is convenient to define this operation symbolically as

$$\mathbb{P}\mathbf{u} \equiv \begin{pmatrix} \psi \\ \nabla^2 \chi \end{pmatrix}, \tag{68}$$

where ψ and χ are the column vectors whose elements are the rational Legendre–Fourier expansion coefficients of $\psi(r, \phi, z)$ and $\chi(r, \phi, z)$ and ∇^2 is the Laplacian operator in matrix form.

In the actual computation of (64) and (65), we exploit fast Fourier transforms to carry out quadratures. In terms of the original valuable μ , they are

$$\begin{aligned} \psi_{mnk} = & \frac{1}{n(n+1)(N_n^m)^2} \int_{-1}^1 \frac{1}{(1-\mu^2)} \left\{ -im P_n^m(\mu) r \tilde{u}_{r,mk}(\mu) \right. \\ & \left. - (1-\mu^2) \frac{dP_n^m(\mu)}{d\mu} r \tilde{u}_{\phi,mk}(\mu) \right\} d\mu \end{aligned} \tag{69}$$

$$\begin{aligned} \chi'_{mnk} = & -\frac{1}{n(n+1)(N_n^m)^2} \int_{-1}^1 \left[\frac{1}{(1-\mu^2)} \left\{ -ik(1-\mu^2) \frac{dP_n^m(\mu)}{d\mu} r \tilde{u}_{r,mk}(\mu) \right. \right. \\ & \left. \left. - mk P_n^m(\mu) r \tilde{u}_{\phi,mk}(\mu) \right\} + n(n+1) P_n^m(\mu) \tilde{u}_{z,mk}(\mu) \right] d\mu \end{aligned} \tag{70}$$

for $n \neq 0$. The χ'_{00k} can be determined by (70) if we substitute $m = 0$ and define $dP_n^0/d\mu \equiv 0$. The ψ_{00k} are determined by (58).

Integrations in (69) and (70) are carried out numerically by the standard Gauss–Legendre quadrature. The number of operations can be reduced in a way similar to (22) and (21) by exploiting the even and odd parity of $P_n^m(\mu)$ and $(1-\mu^2) dP_n^m(\mu)/d\mu$. If the operations in Eqs. (69) and (70) are to be applied to many different vectors, then for efficiency the values of $P_n^m(\mu_i)$ should be stored at each collocation point for $\mu_i < 0$. The values of $(1-\mu_i^2) dP_n^m(\mu_i)/d\mu$ can be computed from the values of $dP_n^m(\mu_i)$ inexpensively [19].

4. EXAMPLES

4.1. Two-Dimensional Quantum Harmonic Oscillator

The Schrödinger equation for a two-dimensional isotropic quantum harmonic oscillator is given in polar coordinates by

$$\frac{d^2 u_n^m(r)}{dr^2} + \frac{1}{r} \frac{du_n^m(r)}{dr} - \frac{m^2}{r^2} u_n^m(r) + (\lambda_n - r^2) u_n^m(r) = 0, \tag{71}$$

where a separation of variable in the azimuthal direction was made by the Fourier modes. The solution is

$$u_n^m(r) \equiv \tilde{N}_n^m r^{|m|} {}_1F_1 \left(-\frac{n-|m|}{2}, |m|+1; r^2 \right) e^{-r^2/2}, \tag{72}$$

where $n \geq |m|$ and $n - |m|$ is even. The ${}_1F_1(a, c; x)$ is the confluent hypergeometric

TABLE II

The Number of Eigenvalues of Eq. (71) That Were Computed Numerically with Eq. (74) That Are within ± 0.05 of Their Exact Values

$M = 10$				$M = 40$				
L	$m = 0$	$m = 3$	$m = 6$	L	$m = 0$	$m = 10$	$m = 20$	$m = 30$
1	2(6)	1(8)	0(-)	1	7(26)	2(26)	0(-)	0(-)
2	3(10)	2(12)	1(14)	2	11(42)	5(38)	1(42)	0(-)
3	4(14)	3(16)	1(14)	4	16(62)	11(62)	7(66)	2(66)
4	3(10)	1(-)	0(-)	8	18(70)	13(70)	7(66)	3(70)
6	1(2)	0(-)	0(-)	12	10(38)	6(42)	2(46)	0(-)
8				16	5(18)	1(22)	0(-)	0(-)

Note. The largest correctly predicted eigenvalue (λ_{\max}) is shown in parentheses.

function and \tilde{N}_n^m is the normalization factor [19]. The ${}_1F_1(-n - |m|/2, |m| + 1; r^2)$ is an even polynomial. The eigenvalue corresponding to $u_n^m(r)$ is

$$\lambda_n = 2(n + 1). \tag{73}$$

Although $u_n^m(r)$ decays exponentially as $r \rightarrow \infty$, the rational Legendre functions can be applied to this problem very efficiently. By changing the variable from r to μ in (71) we obtain

$$[(1 - \mu)\nabla_{\perp}^2(m) - L^2(1 + \mu)] u_n^m(\mu) = -\lambda_n(1 - \mu) u_n^m(\mu). \tag{74}$$

We solve (74) by using the expansion

$$u_n^m(\mu) = \sum_{p=|m|}^M a_p^m P_p^m(\mu). \tag{75}$$

Matrix operators $(1 + \mu)$, $(1 - \mu)$, and $L^2(1 - \mu)^{-s}\nabla_{\perp}^2(m)(1 - \mu)^s$ (including the relevant case with $s = 0$) are given in the Appendix. The Legendre functions are Galerkin (i.e., they are bounded for $-1 \leq \mu \leq 1$), so no boundary condition at infinity need be explicitly imposed.

The truncated problem (74) and (75) has $M - |m| + 1$ eigenvalues. A rule of thumb for eigenproblems solved with spectral methods is that only about half of the eigenvalues are correct [12]. The eigenvalues were computed numerically for $M = 10$ and $M = 40$ for a few choices of m and L . The number and the largest value (λ_{\max}) of eigenvalues which are predicted within ± 0.05 of the exact value tabulated in Table II. The conclusion obtained from the table is that there is an optimum value of L for each M . To see why, note that (27) shows that the resolution of the expansion (75) decreases rapidly for $r > L$. Because $u_n^m(r)$ decays monotonically and rapidly for $r \gtrsim \lambda_n^{1/2}$, the optimum L is expected to occur at $L_{\text{opt}} \sim \lambda_{\max}^{1/2}$. For this value of L the oscillatory part of the eigenfunction will span the high-resolution region $0 \leq r \leq L_{\text{opt}}$. Table II shows that indeed $L_{\text{opt}} \sim 14^{1/2} \approx 3.7$ for

$M = 10$ and $L_{\text{opt}} \sim 70^{1/2} \approx 8.4$ for $M = 40$. The optimum L is nearly independent of m , which is favorable for the unique determination of L_{opt} .

We note that the exact eigenfunctions are square integrable while the eigenfunctions computed using (74) are not necessarily square integrable. To recast the problem so that integrability is explicitly imposed, we define $\hat{u}_n^m(\mu)$ so that $u_n^m(\mu) \equiv (1 - \mu)\hat{u}_n^m(\mu)$ and rewrite (74) as

$$[(1 - \mu) ((1 - \mu)^{-1} \nabla_{\perp}^2(m)(1 - \mu)) - L^2(1 + \mu)] \hat{u}_n^m(\mu) = -\lambda_n(1 - \mu)\hat{u}_n^m(\mu), \quad (76)$$

where (107) in the Appendix with $s = 1$ should be used for the operators in (76). The $\hat{u}_n^m(\mu)$ is expanded by the Legendre functions as in (75). From (19) it is clear the the new eigenfunctions are integrable. In Fig. 1 we show some exact and computed integrable eigenfunctions obtained using (76) for $M = 10$ and $L = 4$. There is a good agreement with the exact solutions.

4.2. Vorticity Equation in Two Dimensions

Next we consider the vorticity equations in two dimensions. Although Lagrangian methods are used in unbounded domains [16–18], our method is Eulerian. The equations of motion are

$$\partial\omega/\partial t + \mathbf{u} \cdot \nabla\omega = 0 \quad (77)$$

$$\omega = \nabla_{\perp}^2\Psi, \quad (78)$$

where

$$\mathbf{u} = (u_r, u_{\phi}) = (-r^{-1}\partial\Psi/\partial\phi, \partial\Psi/\partial r), \quad (79)$$

where $\omega(t, r, \phi)$ is the vorticity and $\Psi(t, r, \phi)$ is the stream function. The vorticity $\omega(t, r, \phi)$ is assumed to decay sufficiently fast so that the stream function $\Psi(t, r, \phi)$ behaves harmonically as $r \rightarrow \infty$. That is, the behavior of the m th azimuthal Fourier components of the stream function is $O(1)$ or $O(\ln(r))$ for $m = 0$ and $O(r^{-|m|})$ for $m \neq 0$ as $r \rightarrow \infty$. The $O(\ln(r))$ behavior results if the circulation Γ , i.e., the integration of vorticity over the entire plane, is not zero. We expand the stream function as

$$\Psi(t, r, \phi) = \Psi_0(t, r, \phi) + \Psi_l P_l(r) + F(r, \phi) \quad (80)$$

$$\Psi_0(t, r, \phi) = \sum_{m=-M}^M \sum_{n=|m|}^M \Psi_n^m(t) P_{L_n}^m(r) e^{im\phi}, \quad (81)$$

where $\Psi_n^m(t)$ and Ψ_l are the expansion coefficients. The Ψ_l is proportional to Γ and is a constant of motion. The $F(r, \phi)$ is the condition imposed on the velocity field as $r \rightarrow \infty$. For example, $F(r, \phi) = Ur \cos(\phi)$ is a uniform freestream velocity field and $F(r, \phi) = Ur^2 \cos(2\phi)$ is a uniform strain field. Here we restrict $F(r, \phi)$ to

$$F(r, \phi) \equiv Ur \cos(\phi). \quad (82)$$

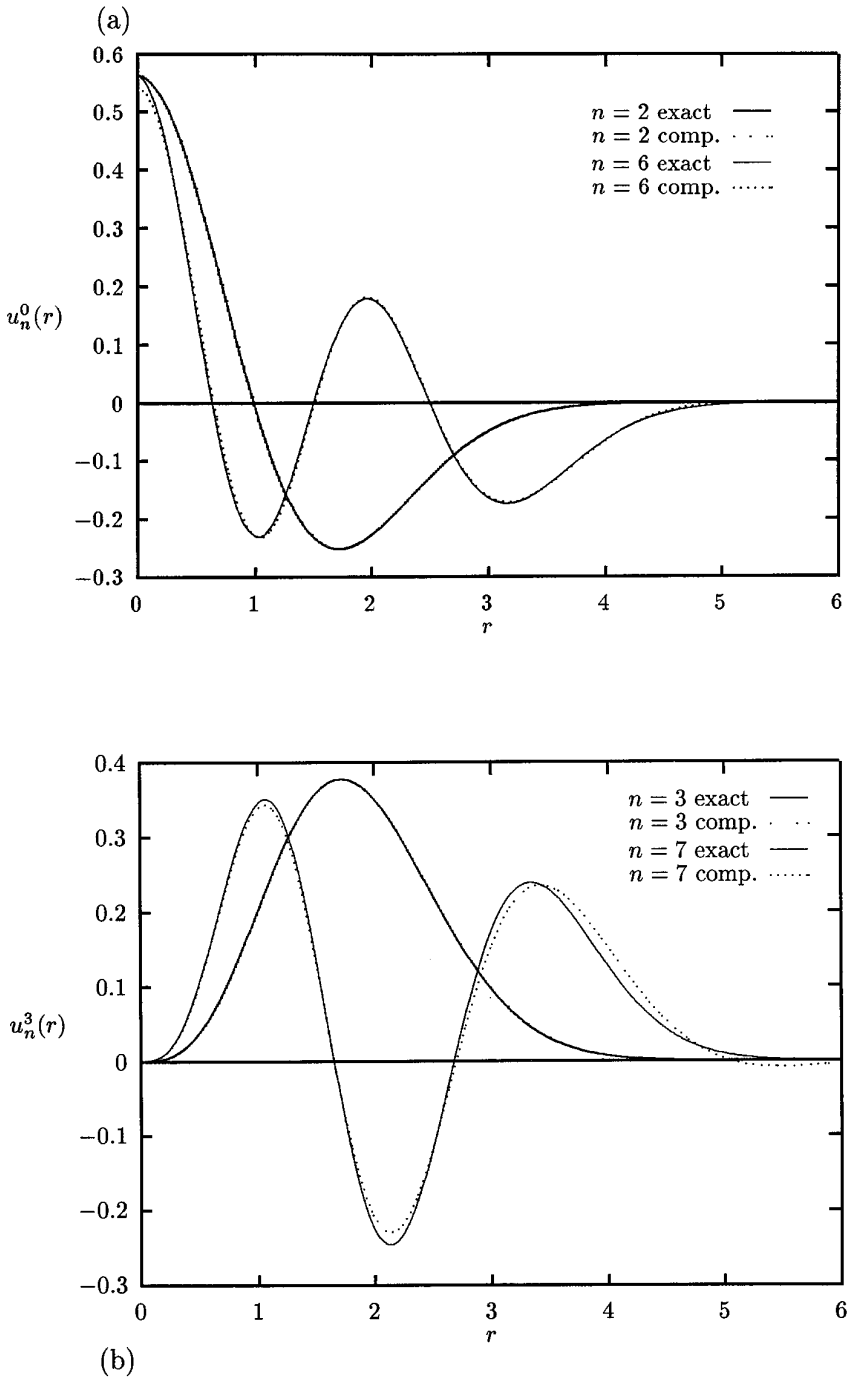


FIG. 1. Plot of exact and computed eigenfunctions of the quantum harmonic oscillator defined in (71). The numerical computations use (76) which enforces integrability. (a) $m = 0$ and (b) $m = 3$. Computational parameters are $M = 10$, $L = 4$.

Defining

$$\omega(t, r, \phi) \equiv 4L^4(L^2 + r^2)^{-2}\hat{\omega}(t, r, \phi) \tag{83}$$

with

$$\hat{\omega}(t, r, \phi) = \sum_{m=-M}^M \sum_{n=|m|}^M \hat{\omega}_n^m(t) P_{Ln}^m(r) e^{im\phi}, \tag{84}$$

and applying the Laplacian operator to (80), we obtain

$$\hat{\omega}_n^m(t) = -n(n + 1)\Psi_n^m(t)/L^2, \quad n \neq 0 \tag{85}$$

$$\hat{\omega}_0^0(t) = \Psi_l/L^2, \quad n = 0, \tag{86}$$

where we have used (10) and $P_{L_0}^0(r) \equiv 1$. Thus it is trivial to compute $\hat{\omega}_n^m(t)$ from $\Psi_n^m(t)$ and Ψ_l . To compute the stream function from $\hat{\omega}(t, r, \phi)$, we simply invert (85) and (86) to find Ψ_l and $\Psi_n^m(t)$. The indeterminate term $\Psi_0^0(t)$ is a gauge which can be set arbitrarily.

In terms of μ and ϕ , (77) becomes

$$\begin{aligned} \frac{\partial \hat{\omega}}{\partial t} = & -\frac{1 - \mu}{L^2(1 + \mu)} \left\{ \left((1 - \mu^2) \frac{\partial}{\partial \mu} (\Psi_0 + F) + (1 + \mu)\Psi_l \right) \left(\frac{\partial \hat{\omega}}{\partial \phi} \right) \right. \\ & \left. - \left((1 - \mu^2) \frac{\partial \hat{\omega}}{\partial \mu} - 2(1 + \mu)\hat{\omega} \right) \left(\frac{\partial}{\partial \phi} (\Psi_0 + F) \right) \right\}. \end{aligned} \tag{87}$$

To compute the right-hand side of (87), the operators $(1 - \mu^2)(\partial/\partial\mu)$, $(1 + \mu)$, and $\partial/\partial\phi$ are applied to Ψ_0 and $\hat{\omega}$ in the function space (i.e., the matrix operators given in the Appendix are applied to Ψ_n^m and $\hat{\omega}_n^m$), and then the results are transformed (and possibly dealiased) from function space to physical space (i.e., evaluated at the collocation points). The multiplication of terms within the curly brackets should be done in physical space. The multiplication by $1/(1 + \mu)$ on the right-hand side of (87) should also be carried out in physical space. If the multiplication were in function space and if the transformation from function to physical space were dealiased, then the product would no longer be exactly divisible by $(1 + \mu)$, so the product might no longer be integrable (see (19)). On the other hand, the multiplication by $(1 - \mu)$ on the right-hand side of (87) should be carried out last and be done in function space after dealiasing in order to maintain the condition $\partial\hat{\omega}/\partial t|_{r=\infty} = 0$. This condition is important for the accurate conservation of angular momentum.

To illustrate the solution of (77) using this method, we consider an initial condition consisting of a vortex pair

$$\omega(0, x, y) = -G(x + b/2, y) + G(x - b/2, y), \tag{88}$$

where

$$G(x, y) \equiv A \exp(-0.5A(x^2 + y^2)), \tag{89}$$

TABLE III
Induced Velocity u_1 of the Vortex Pair Described in Section 4.2 and the Fractional
Change of Enstrophy ΔEN at $t = 5$

A	$2r_0$	u_1	ΔEN
32	0.500	0.95538	-1.36×10^{-3}
64	0.353	0.99120	-6.63×10^{-4}
128	0.250	0.99767	-1.60×10^{-4}
256	0.177	0.99920	-3.96×10^{-5}
512	0.125	1.00844	-1.24×10^{-3}

where $x \equiv r \cos \phi$ and $y \equiv r \sin \phi$. The circulation associated with $G(x, y)$ is $\Gamma = 2\pi$ and the vortex core radius is $r_0 \equiv (2/A)^{1/2}$. For sufficiently large A , the point vortex approximation holds and the vortex pair descends downward with velocity $u_y \approx -\Gamma/(2\pi b) = -1/b$. Because the vorticity is localized in two regions both at $r \sim b/2$, the map parameter L should be chosen to maximize the resolution at $r \sim b/2$. From (27),

$$\frac{\partial X_L}{\partial L} = \frac{8L(r^2 - L^2)}{(r^2 + L^2)^3} \quad (90)$$

so that the maximum resolution at $r = b/2$ is attained when $L = b/2$. The computational parameters are chosen as $b = 1$, $L = 0.5$, and $M = 42$. We set $U = 1$ in (82) so that the vortex pair nearly remains at the original location. Equation (87) was integrated with a leap frog method with time step $\Delta t = 0.001$. No stiffness is observed in our method despite the presence of the coordinate singularity [1]. A simplified hyperviscosity was used to prevent the enstrophy pile up to the small scale.

To estimate the translation velocity of the vortex pair, we define the position of the vortex pair \bar{y} as

$$\bar{y}(t) \equiv \frac{1}{\text{EN}} \int_{\phi=0}^{2\pi} \int_{r=0}^{\infty} r \sin \phi \omega^2 r \, dr \, d\phi, \quad (91)$$

where EN is the enstrophy

$$\text{EN} \equiv \int_{\phi=0}^{2\pi} \int_{r=0}^{\infty} \omega^2 r \, dr \, d\phi. \quad (92)$$

Note that $\bar{y}(0) = 0$. We defined the induced velocity u_1 in the y direction as $u_1 \equiv \mathbf{z} \times \nabla F(r, \phi) - \bar{y}(t)/t = 1 - \bar{y}(t)/t$. In Table III we show u_1 and the fractional change of EN at $t = 5$ for several computations with different values of A . If the vortices were points and if there were no numerical errors, then u_1 would be unity for all time. In reality, the finite-area vortices become slightly elliptical with major axes parallel to the y -axis. However, no significant vorticity filamentation occurs and the enstrophy is numerically approximately conserved. For smaller A the enstrophy decay is slightly larger due to the unsteadiness before the vortices adjust to an

elliptical shape. As r_0 becomes smaller, the point vortex approximation becomes more accurate. However, for $A = 512$, the r_0 is too small to be numerically resolved properly, and the result is less accurate as indicated in the larger decay of the enstrophy. For $A \leq 256$, the u_1 is smaller than the point vortex approximation and the behavior is consistent with the calculations by Pierrehumbert [29] and Wu *et al.* [30], who considered a pair of uniform vorticity regions.

4.3. Vorticity Equation in Three Dimensions

We consider the motion of vortex filaments in an unbounded domain. The equations of motion for the vortex filaments are

$$\partial \mathbf{u} / \partial t = -\boldsymbol{\omega} \times \mathbf{u} - \nabla \Pi + \mathcal{D} \mathbf{u} \tag{93}$$

$$\nabla \cdot \mathbf{u} = 0, \tag{94}$$

where \mathbf{u} is the velocity and $\boldsymbol{\omega} \equiv \nabla \times \mathbf{u}$ is the vorticity. The $\mathcal{D} \mathbf{u}$ is the linear dissipation term to be defined later and Π is the dynamic pressure. Applying the projection operator defined in (68) to (93), we obtain

$$\partial \mathbb{P} \mathbf{u} / \partial t = -\mathbb{P}(\boldsymbol{\omega} \times \mathbf{u}) + \mathbb{P} \mathcal{D} \mathbf{u}. \tag{95}$$

The linear problem is defined by

$$-i\sigma \mathbb{P} \mathbf{u}_1(r) = \mathbb{P}(-\bar{\boldsymbol{\omega}}(r) \times \mathbf{u}_1(r) + \bar{\mathbf{u}}(r) \times \boldsymbol{\omega}_1(r)) + \mathbb{P} \mathcal{D} \mathbf{u}_1(r) \tag{96}$$

$$\mathbf{u} = \bar{\mathbf{u}}(r) + \mathbf{u}_1(r) e^{im\phi + ikz - i\sigma t} \tag{97}$$

$$\boldsymbol{\omega} = \bar{\boldsymbol{\omega}}(r) + \boldsymbol{\omega}_1(r) e^{im\phi + ikz - i\sigma t}, \tag{98}$$

where $\bar{\mathbf{u}}(r)$ and $\bar{\boldsymbol{\omega}}(r)$ are unperturbed velocity and vorticity profiles and $\mathbf{u}_1(r)$ and $\boldsymbol{\omega}_1(r)$ denote their perturbations. The \mathbb{P} and \mathcal{D} in (96) are the operators for the m th azimuthal Fourier component and axial wavenumber k . The toroidal and poloidal decomposition is applied to velocity field \mathbf{u} as described in Section 3.2.

First we consider the linear problem (96) with unperturbed velocity

$$\bar{\mathbf{u}}(r) = (0, q(1 - e^{-r^2})/r, h e^{-\beta r^2}). \tag{99}$$

Recently, Mayer and Powell [11] considered the linear stability of (99) (with $h = \beta = 1$) for viscous and inviscid cases by using the Chebyshev spectral method. An eigenvalue computation result for a viscous problem ($\mathcal{D} = \text{Re}^{-1} \nabla^2$) is shown in

TABLE IV

Comparison of the Convergence Rate of the Eigenvalues of the Most Unstable Eigenmode with $m = 1$, $k = 0.05$ of the Columnar Vortex Given by (99) with $q = 0.5$ $h = 1$, $\beta = 1$, and $Re = 25$

Present study		
M	L	Eigenvalue σ
10	4	$-0.0022047741 + i0.00101433703$
20	6	$-0.0022387022 + i0.00098862812$
30	7	$-0.0022386899 + i0.00098851096$
40	8	$-0.0022387038 + i0.00098851652$
50	11	$-0.0022387039 + i0.00098851647$
60	12	$-0.0022387039 + i0.00098851644$
70	13	$-0.0022387039 + i0.00098851644$

Mayer and Powell		
M	R	Eigenvalue σ
50	100	$0.0008264638 + i0.00391478239$
75	110	$-0.0020054328 + i0.00098616247$
100	120	$-0.0022341283 + i0.00098890815$
150	140	$-0.0022387165 + i0.00098851641$
200	160	$-0.0022387036 + i0.00098851650$
250	180	$-0.0022387038 + i0.00098851655$
300	200	$-0.0022387039 + i0.00098851643$

Note. R is the radius at which Mayer and Powell imposed their outer boundary conditions. M is the number of radial modes per variable.

Table IV to compare the efficiency of our method with that of Mayer and Powell. The number of coefficients for each variable is M . The order of linear system is $2M$ for our method and $3M$ for that of Mayer and Powell. Clearly more accuracy is attained in our method with a smaller value of M . The difference in efficiency is especially clear for small axial wavenumbers for which the eigenfunctions decay slowly for large r .

As another example application, we consider the neutrally stable oscillations of a columnar vortex with (99), with no dissipation ($\mathcal{D} = 0$), and with perturbations of the form (97). In the long wavelength limit, the eigenvalues can be computed analytically by using Moore and Saffman’s asymptotic formula (Eq. (7.2) in [31]). (See [37] for details.) The analytic expression for the eigenvalue is

$$\sigma_r/q = -(k^2/2)\{-\ln k - (\gamma - \ln 2)/2 - h^2/2q^2\beta - hk/(q\beta + q\beta^2)\}/(1 + hk/q\beta) \tag{100}$$

with $\sigma_i \equiv 0$, where $\sigma \equiv \sigma_r + i\sigma_i$ and $\gamma = 0.57721566 \dots$ is Euler’s constant. Widnall *et al.* [32] obtained a result similar to (100). However, their result does not contain the terms with the first power of h in (100) and is less accurate when h is not zero.

We compare the eigenvalues computed with our numerical method (with $\mathcal{D} =$

TABLE V

Comparison of the Numerically Computed Real Parts σ_r of the Eigenvalues ($\sigma_i \equiv 0$) of the Eigenmodes of the Columnar Vortex Described in Section 4.3 with the Asymptotic Form Given in (100)

No.	k	h/q	β	L_{opt}	σ_r/q	
					Numerical value	Eq. (100)
1	0.4	0.0	—	10	-8.970×10^{-2}	-7.794×10^{-2}
2	0.2	0.0	—	11	-3.441×10^{-2}	-3.335×10^{-2}
3	0.1	0.0	—	12	-1.189×10^{-2}	-1.180×10^{-2}
4	0.05	0.0	—	13	-3.824×10^{-3}	-3.817×10^{-3}
5	0.025	0.0	—	15	-1.171×10^{-3}	-1.171×10^{-3}
6	0.025	2.0	1.0	12	-5.127×10^{-4}	-5.125×10^{-4}
7	0.025	1.0	1.0	13	-9.865×10^{-4}	-9.861×10^{-4}
8	0.025	-1.0	1.0	14	-1.045×10^{-3}	-1.045×10^{-3}
9	0.025	-2.0	1.0	13	-5.832×10^{-4}	-5.828×10^{-4}
10	0.025	2.0	0.5		***	9.086×10^{-5}
11	0.025	1.0	0.5	14	-8.081×10^{-4}	-8.076×10^{-4}
12	0.025	-1.0	0.5	15	-9.150×10^{-4}	-9.145×10^{-4}
13	0.025	-2.0	0.5		***	6.475×10^{-5}
14	0.025	2.0	2.0	9	-8.353×10^{-4}	-8.349×10^{-4}
15	0.025	1.0	2.0	11	-1.078×10^{-3}	-1.078×10^{-3}
16	0.025	-1.0	2.0	11	-1.108×10^{-3}	-1.108×10^{-3}
17	0.025	-2.0	2.0	9	-8.835×10^{-4}	-8.831×10^{-4}

Note. The *** indicates that no negative eigenvalues were obtained.

0) and (100) in Table V. In our method, $M = 59$ was used and the optimum map parameter L_{opt} was determined as the value at which σ_r is least sensitive to L . The L_{opt} is about one order larger than the unperturbed vortex core radius and becomes larger as k becomes smaller, reflecting the slower decay of the eigenfunctions for larger r . Thus the problem becomes increasingly difficult for smaller k because the basis functions have to resolve both the unperturbed profiles and the eigenfunctions simultaneously. However, Table V shows a range of k where the numerical results agree well with the asymptotic form (100). Agreement becomes better as k becomes smaller as expected (run Nos. 1–5) and remains good even if the axial flow is present (run Nos. 6–17).

The final example of our numerical method is the solution of the nonlinear initial value problem (95). It illustrates the robustness of our method. To confine the effect of dissipation to small scale, we use a hyperviscosity ($\mathcal{D} = -\nu_4 \nabla^4$). Equation (95) can be rewritten as

$$\begin{pmatrix} \partial \psi / \partial t \\ \nabla^2 \partial \chi / \partial t \end{pmatrix} = -\mathbb{P}(\boldsymbol{\omega} \times \mathbf{u}) - \nu_4 \begin{pmatrix} \nabla^4 \psi \\ \nabla^6 \chi \end{pmatrix}. \quad (101)$$

We solve (101) by the fractional step method using the Adams–Bashforth method

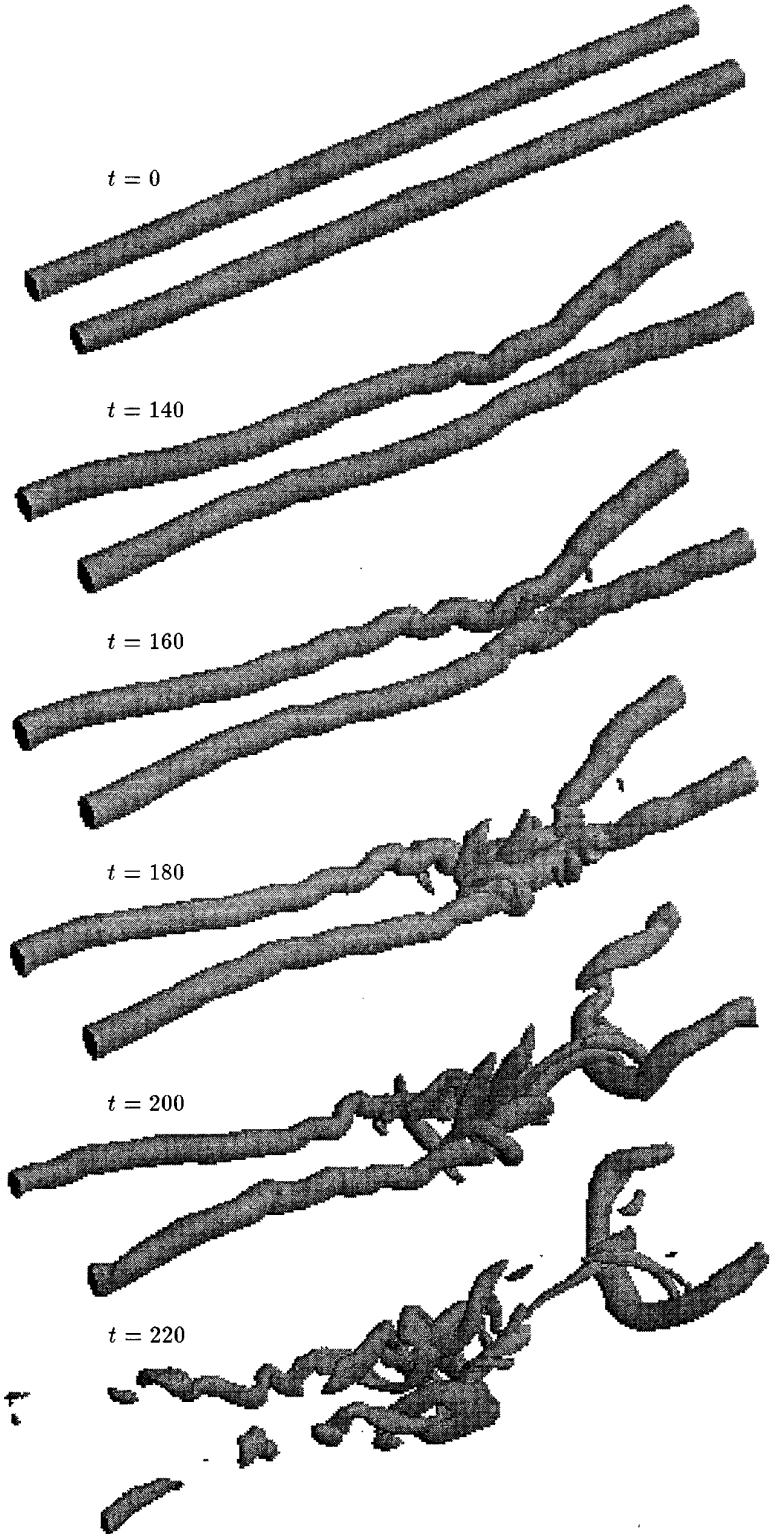


FIG. 2. Isovorticity surface of the vortex pair. $|\omega| = 0.75$. See text for description of the initial condition.

for the nonlinear term and the backward Euler method for the dissipation term. The toroidal and poloidal components are decoupled in the second step. The Crank–Nicholson method can be applied for the dissipation term if more accuracy is desired. A result is shown in Fig. 2. Two vortex filaments are positioned initially parallel to the z -axis with a separation of six units. The computation is axially periodic with an axially domain length of 50 units. Each vortex has the velocity profile (99) with $q = \pm 1$ and $h = 0$. The signs of q are determined so that the vortex pair descends downward. The vortices are perturbed randomly at $t = 0$ and the initial value problem was solved until $t = 220$ in 2200 time steps. A uniform upward velocity field was imposed to keep the vortex pair in the well-resolved computational region. Vorticity far away from the origin was removed periodically to continue the computation stably. This causes a few percent loss of circulation and axial momentum at the end of the computation. (When this vorticity is not removed, these quantities are conserved exactly, but the calculation eventually blows up.) The computation has $|m| \leq 40$, $n \leq 40$, and $|k| \leq 83$ in (48)–(53). Other computational parameters are $L = 5.5$ and $\nu_4 = 7 \times 10^{-4}$. Hyperviscosity was turned on after $t = 80$.

The vortices clearly show the long wavelength Crow instability [33] as well as a faster growing short wavelength instability. Two filaments touch at $t \sim 160$ and the bridging [34] associated with the reconnection is observed at $t = 200$. The vortices dissipate quickly after $t = 200$.

Our method is efficient for this geometry compared to Fourier methods which assume periodicity in the x - and y -directions [35, 36]. In those methods, domain lengths in the x - and y -directions that are large compared to the vortex filaments' separation must be used to avoid effects of the artificial periodic array of vortices created by the periodic basis functions. Thus only a fraction of the collocation points can be used actively in those computations.

APPENDIX

For a function $f_m(\mu)$ expanded with coefficients a_n^m as

$$f_m(\mu) = \sum_{n=|m|}^{\infty} a_n^m P_n^m(\mu), \quad (102)$$

we consider the function $g_m(\mu) \equiv \mathcal{L}f_m(\mu)$ expanded with coefficients b_n^m so that

$$g_m(\mu) = \mathcal{L}f_m(\mu) = \sum_{n=|m|}^{\infty} b_n^m P_n^m(\mu). \quad (103)$$

In the following formulas, we assume $a_n^m \equiv 0$ if $n < |m|$.

$$\text{If } \mathcal{L} = (1 - \mu^2) \frac{\partial}{\partial \mu} = r \frac{d}{dr},$$

$$b_n^m = -\frac{(n-1)(n-|m|)}{2n-1} a_{n-1}^m + \frac{(n+2)(n+|m|+1)}{2n+3} a_{n+1}^m. \quad (104)$$

$$\text{If } \mathcal{L} = 1 + \mu = \frac{2r^2}{r^2 + L^2},$$

$$b_n^m = \frac{n-|m|}{2n-1} a_{n-1}^m + a_n^m + \frac{n+|m|+1}{2n+3} a_{n+1}^m. \quad (105)$$

$$\text{If } \mathcal{L} = 1 - \mu = \frac{2L^2}{r^2 + L^2},$$

$$b_n^m = -\frac{n-|m|}{2n-1} a_{n-1}^m + a_n^m - \frac{n+|m|+1}{2n+3} a_{n+1}^m. \quad (106)$$

If $\mathcal{L} = L^2(1 - \mu)^{-s} \nabla_{\perp}^2(m)(1 - \mu)^s$, where $\nabla_{\perp}^2(m)$ is defined by (14) and s is an integer,

$$\begin{aligned} b_n^m = & -\frac{(n-|m|-1)(n-|m|)(n-2+s)(n-1+s)}{(2n-3)(2n-1)} a_{n-2}^m \\ & + \frac{2n(n-|m|)(n-1+s)}{(2n-1)} a_{n-1}^m \\ & + \frac{1}{(2n-1)(2n+3)} \{-2n(n+1)(3n^2+3n-m^2-2) \\ & + 2s(s-2)(n^2+n+m^2-1)\} a_n^m \\ & + \frac{2(n+1)(n+|m|+1)(n+2-s)}{(2n+3)} a_{n+1}^m \\ & - \frac{(n+|m|+1)(n+|m|+2)(n+3-s)(n+2-s)}{(2n+3)(2n+5)} a_{n+2}^m. \end{aligned} \quad (107)$$

REFERENCES

1. T. Matsushima and P. S. Marcus, *J. Comput. Phys.* **120**, 365 (1995).
2. G. H. Rawitscher, *J. Comput. Phys.* **94**, 81 (1991).
3. C. E. Grosch and S. A. Orszag, *J. Comput. Phys.* **25**, 273 (1977).
4. J. P. Boyd, *J. Comput. Phys.* **45**, 43 (1982).
5. P. R. Spalart, R. D. Moser, and M. M. Rogers, *J. Comput. Phys.* **96**, 297 (1991).
6. R. D. Moser and M. M. Rogers, *J. Fluid Mech.* **247**, 275 (1993).
7. J. P. Boyd, *Chebyshev & Fourier Spectral Methods* (Springer-Verlag, Berlin, 1989).
8. J. A. C. Weideman and A. Cloot, *Comput. Methods Appl. Mech. Eng.* **80**, 467 (1990).
9. J. P. Boyd, *J. Comput. Phys.* **110**, 360 (1994).
10. M. R. Khorrami, *J. Fluid Mech.* **225**, 197 (1991).
11. E. W. Mayer and K. G. Powell, *J. Fluid Mech.* **245**, 91 (1992).
12. J. P. Boyd, *J. Comput. Phys.* **70**, 63 (1987).
13. S. Chandrasekhar, *Hydrodynamic and Hydromagnetic Stability* (Dover, New York, 1961).

14. P. S. Marcus, *Astrophys. J.* **231**, 176 (1979).
15. G. A. Glatzmaier, *J. Comput. Phys.* **55**, 461 (1984).
16. A. J. Chorin, *J. Fluid Mech.* **57**, 785 (1973).
17. J. Strain, *J. Comput. Phys.* **124**, 131 (1996).
18. J. Strain, *J. Comp. Phys.* **132**, 108 (1997).
19. M. Abramowitz and I. A. Stegun, *Handbook of Mathematical Functions* (Dover, New York, 1964).
20. D. Gottlieb and S. A. Orszag, *Numerical Analysis of Spectral Methods: Theory and Applications* (SIAM, Philadelphia, 1977).
21. W. H. Press, S. A. Teukolsky, W. T. Vetterling, and B. P. Flannery, *Numerical Recipes*, 2nd ed. (Cambridge Univ. Press, Cambridge, England, 1992).
22. L. V. Ahlfors, *Complex Analysis*, 3rd ed. (McGraw-Hill, New York, 1979).
23. S. A. Orszag, *Mon. Weather Rev.* **102**, 56 (1974).
24. A. B. Cain, J. H. Ferziger, and W. C. Reynolds, *J. Comput. Phys.* **56**, 272 (1984).
25. J. P. Boyd, *J. Comput. Phys.* **69**, 112 (1987).
26. A. J. Robert, *J. Meteorol. Soc. Jpn.* **44**, 237 (1966).
27. A. T. Patera and S. A. Orszag, In *Proceedings, Nonlinear Problems: Present and Future* (North-Holland, Amsterdam, 1982), p. 367.
28. A. Leonard and A. Wray, in *Proceedings, Ninth International Conference on Numerical Methods in Fluid Mechanics, Aachen, 1982*.
29. R. T. Pierrehumbert, *J. Fluid Mech.* **99**, 129 (1980).
30. H. M. Wu, E. A. Overman II, and N. J. Zabusky, *J. Comput. Phys.* **53**, 42 (1984).
31. D. W. Moore and P. G. Saffman, *Philos. Trans. R. Soc. London Ser. A* **272**, 403 (1972).
32. S. E. Widnall, D. Bliss, and A. Zalay, in *Aircraft Wake Turbulence and Its Detection* (Plenum, New York, 1971), p. 305.
33. S. C. Crow, *AIAA J.* **8**, 2172 (1970).
34. S. Kida and M. Takaoka, *Annu. Rev. Fluid Mech.* **26**, 169 (1994).
35. R. Corral and J. Jiménez, *J. Comput. Phys.* **121**, 261 (1995).
36. P. R. Spalart, *J. Fluid Mech.* **327**, 139 (1996).
37. T. Matsushima, *Spectral Methods in Polar Coordinates with an Application to the Stability of a Trailing Vortex*, Ph.D. thesis, University of California at Berkeley, 1995.